

Progress in Diamond Detector Development

R. Wallny,^{b,1,*} M. Artuso,^a L. Bäni,^b V. Bellini,^c B. Bentele,^d P. Bergonzo,^e
 A. Bes,^f J-M. Brom,^g G. Chiodini,^h D. Chren,ⁱ V. Cindro,^j G. Claus,^g J. Collot,^f
 J. Cumalat,^d A. Dabrowski,^k D. Dauvergne,^f S. Ditalia Tchernij,^l G. Eigen,^m
 V. Eremin,ⁿ P. Everaere,^f J. Forneris,^l L. Gallin-Martel,^f M-L. Gallin-Martel,^f
 K.K. Gan,^o M. Gastal,^l A. Gentry,^p M. Goffe,^g J. Goldstein,^q A. Gorišek,^j
 J. Grosse-Knetter,^r B. Hiti,^j D. Hits,^b C. Hoarau,^f M. Hoferkamp,^p J. Hosselet,^g
 F. Hügging,^s C. Hutson,^q R. Jackman,^e R. Jennings-Moors,^e H. Kagan,^o
 K. Kanxheri,^t M. Kis,^u G. Kramberger,^j M. Kruger,^v A. Lacoste,^f E. Lukosi,^w
 C. Maazouzi,^g M. Mali,^j I. Mandić,^j S. Marcatili,^f A. Marino,^d C. Mathieu,^g
 M. Menichelli,^t M. Mikuz,^j R. Molle,^f A. Morozzi,^t F. Moscatelli,^t J. Moss,^x
 R. Mountain,^a J-F. Muraz,^f E.A. Narazyanan,^p A. Oh,^y P. Olivero,^m D. Passeri,^t
 H. Pernegger,^k R. Perrino,^h F. Picollo,^l A. Porter,^y A. Portier,^f R. Potenza,^c
 A. Quadt,^r F. Rarbi,^f A. Re,^l M. Reichmann,^b S. Roe,^k O. Rossetto,^f P. Salter,^v
 D.A. Sanz Becerra,^b C. Schmidt,^u S. Schnetzer,^z S. Seidel,^p L. Servoli,^t
 R. Shivaraman,^v S. Smith,^o B. Sopko,ⁱ V. Sopko,ⁱ J. Sorenson,^p S. Spagnolo,^h
 S. Spanier,^w K. Stenson,^d R. Stone,^z B. Stugu,^m C. Sutura,^c M. Traeger,^u
 W. Trischuk,^{zz} M. Truccato,^l C. Tuve,^c J. Velthuis,^q E. Verbitskaya,ⁿ S. Wagner,^d
 J. Welch,^e T. Wengler,^k M. Yamouni,^f J. Zalieckas^m and M. Zavrtnik^j

^aSyracuse University, Syracuse, NY, USA

^bETH Zürich, Zürich, Switzerland

^cINFN/University of Catania, Catania, Italy

^dUniversity of Colorado, Boulder, CO, USA

^eUniversity College London, London, UK

^fLPSC-Grenoble, Grenoble, France

^gIPHC, Strasbourg, France

^hINFN-Lecce, Lecce, Italy

ⁱCzech Technical Univ., Prague, Czech Republic

^jJožef Stefan Institute, Ljubljana, Slovenia

^kCERN, Geneva, Switzerland

^lUniversity of Torino, Torino, Italy

^mUniversity of Bergen, Bergen, Norway

ⁿAffiliated with an institute covered by a cooperation agreement with CERN

¹For the RD42 collaboration.

*Speaker

- ^oThe Ohio State University, Columbus, OH, USA
^pUniversity of New Mexico, Albuquerque, NM, USA
^qUniversity of Bristol, Bristol, UK
^rUniversität Goettingen, Goettingen, Germany
^sUniversität Bonn, Bonn, Germany
^tNFN-Perugia, Perugia, Italy
^uGSI, Darmstadt, Germany
^vUniversity of Oxford, Oxford, UK
^wUniversity of Tennessee, Knoxville, TN, USA
^xCalifornia State University - Sacramento, USA
^yUniversity of Manchester, Manchester, UK
^zRutgers University, Piscataway, NJ, USA
^{zz}University of Toronto, Toronto, ON, Canada

Detectors based on Chemical Vapor Deposition (CVD) diamond have been used successfully in Luminosity and Beam Condition Monitors (BCM) in the highest radiation areas of the LHC. Future experiments at CERN will accumulate an order of magnitude larger fluence. As a result, an enormous effort is underway to identify detector materials that can operate under fluences of $1 \cdot 10^{16}$ n cm⁻² and $1 \cdot 10^{17}$ n cm⁻². Diamond is one candidate due to its large displacement energy that enhances its radiation tolerance. Over the last 30 years the RD42 collaboration has constructed diamond detectors in CVD diamond with a planar geometry and with a 3D geometry to extend the material's radiation tolerance. The 3D cells in these detectors have a size of 50 μm×50 μm with columns of 2.6 μm in diameter and 100 μm×150 μm with columns of 4.6 μm in diameter. Here we present the latest beam test results from planar and 3D diamond pixel detectors.

1. Introduction

Diamond detectors have firmly established themselves in particle physics experiments. For more than two decades they have been utilized as luminosity monitors, beam condition monitors, and beam protection devices for a number of high energy experiments [1–5].

Among the big advantages of diamond particle detectors are their simplicity and robustness. A typical diamond detector consists of a flat piece of diamond produced by Chemical Vapor Deposition (CVD) with two metal contacts on each side to which an external bias is applied. This arrangement forms a solid state ionization chamber. A charged particle passing through creates electron-hole pairs, whose drift under the applied electric field induces a signal which is then registered by the front-end electronics.

Although the large band gap of diamond results in signals smaller than those in silicon devices of the same thickness, it does prevent large ($> \text{few nA}$) leakage currents. This allows for diamonds to be used without external cooling and even at elevated temperatures. It also, together with low dielectric constant, results in low noise in the detector.

Another advantage of CVD diamonds is their high radiation tolerance. The RD42 collaboration has measured the signal dependence of diamond detectors as a function of exposure to fluence by a large variety of the damage inducing particles up to the fluences of $7 \cdot 10^{16} \text{ n cm}^{-2}$ [6, 7]. It was found that diamond, in comparison to silicon, is more radiation tolerant against proton irradiation and has similar radiation tolerance against neutrons.

In high energy experiments the detectors experience a wide range of particle fluxes. For example, the rate of particles during a Van der Meer scan is much lower than during a physics run. It is important that the operation of the detectors is not affected by the changing flux. The RD42 collaboration has tested polycrystalline CVD (pCVD) diamonds in a range of particle fluxes from a few kHz cm^{-2} to a few MHz cm^{-2} . It was determined that although non-irradiated pCVD diamond detectors do show a small ($<5\%$) change in pulse height within that flux range, the dependence completely disappears after exposure to a small fluence of neutrons, as can be seen in Figure 1 [8].

Parker et al. [9] have shown that the radiation tolerance of a detector can be further enhanced by placing bias and readout electrodes within the bulk of the sensitive detector material, perpendicular to its surface. Such arrangement of the electrodes allows for them to be placed closer than the mean distance charge carriers drift before capture or recombination ("schubweg") at the expected maximum fluence experienced by a detector in a high energy experiment. The devices with this arrangement of electrodes are called 3D detectors. The RD42 collaboration has developed and studied a prototype of a 3D detector based on a single crystal CVD diamond. It was shown that this detector collects a comparable amount of charge to a detector with surface electrodes, but at a significantly smaller bias voltage [10]. In these proceedings we show results of beam test studies of two recent 3D detectors based on pCVD diamonds with pixel readout.

2. Experimental Setup

The 3D detectors were constructed from two pCVD diamond sensors with dimensions of $5 \text{ mm} \times 5 \text{ mm}$ and thickness of $500 \mu\text{m}$. The diamond sensors were preselected to have low leakage current ($<1 \text{ nA}$) and charge collection distance (CCD) larger than $250 \mu\text{m}$ at 1000 V bias. The

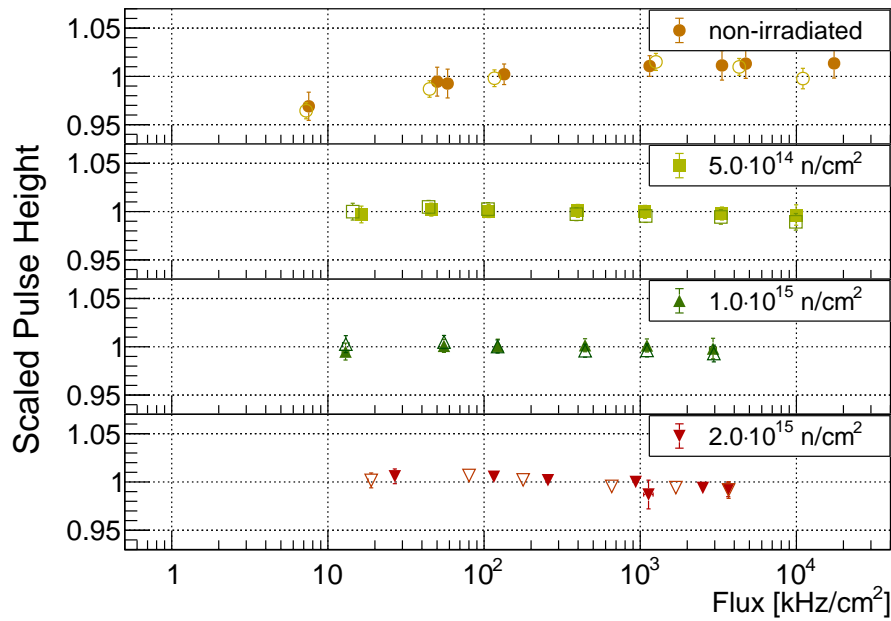


Figure 1: The dependence of the scaled average pulse height on a particle flux. The filled markers are for the measurements with the positive bias on the detector and the open markers are for the measurements with the negative bias on the detector.

3D electrodes were formed with a femtosecond laser using the procedure developed by P. Salter et al. [11]. The procedure converts diamond into a resistive mixture of carbon phases within a focal point of the laser. The diamond is passed through the laser focal point and a thin (few μm) column is formed within the diamond bulk. The thickness of the electrodes in the detector with $50\ \mu\text{m} \times 50\ \mu\text{m}$ cells was approximately $2.6\ \mu\text{m}$ while the thickness of the electrodes in the detector with $100\ \mu\text{m} \times 150\ \mu\text{m}$ cells was approximately $4.6\ \mu\text{m}$. The column production efficiency reached 99.7%. In both devices the electrodes are drilled from one side down to a distance of $15\ \mu\text{m}$ away from the other side. The bias and the readout electrodes start at opposite sides. The bias side of each detector corresponded to the substrate side of the diamond and the readout to the growth side of the diamond. The bias and readout electrodes are periodically arranged in rectangular structures (cells). A cell consisted of a readout electrode surrounded by four bias electrodes. The cell dimensions of one detector were $50\ \mu\text{m} \times 50\ \mu\text{m}$ while the dimensions of the other were $100\ \mu\text{m} \times 150\ \mu\text{m}$. The 3D electrodes on the bias side of both detectors were all ganged together by a Cr/Au metallization. On the readout side of the detector with $50\ \mu\text{m} \times 50\ \mu\text{m}$ cells, six readout electrodes were ganged together with TiW metallization in order to match the pitch of the readout chip (ROC) (see Figure 2a). Each readout electrode of the detector with $100\ \mu\text{m} \times 150\ \mu\text{m}$ cells was individually connected by a TiW metallization to the bump pad (see Figure 2b).

After the surface metallization, each detector was bump bonded [12] to a *PSI46digV2.1respin* ROC [13]. Indium columns, $7\ \mu\text{m}$ thick, were deposited on the bump pads of the sensor and the readout chip. The sensor was then flipped, the indium columns of the sensor and the readout chip aligned and pressed together at room temperature forming a bond. No reflow was performed. Figure 3 shows a photograph of an assembled detector and a cross section of a schematic of the

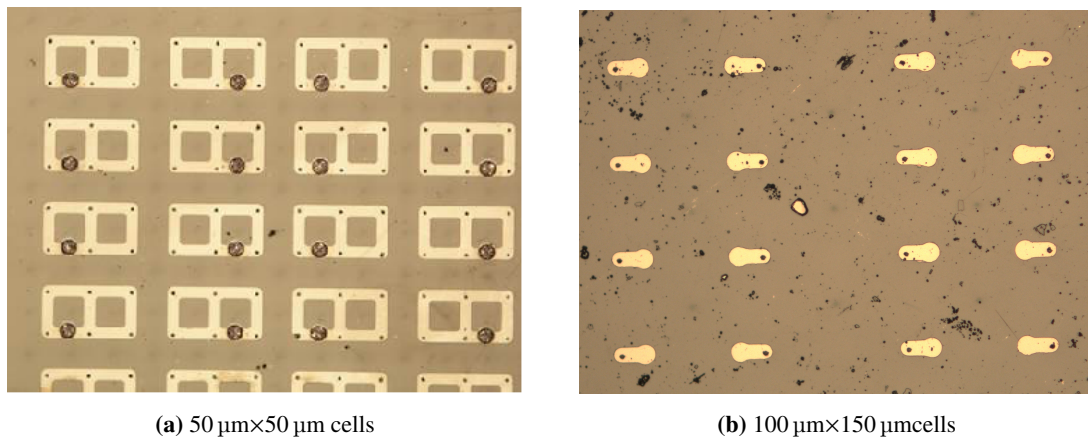


Figure 2: Readout metallization patterns for 50 μm ×50 μm (left) 100 μm ×150 μm (right). On the left picture the indium columns can be observed. The black dots seen in the (pale yellow) metal are the readout columns. The bias columns are 15 μm below the surface and only faintly visible.

bump bonded device. The cross section schematic visually clarifies the arrangement of the bias and readout columns, the metallization, and the bump bonding.

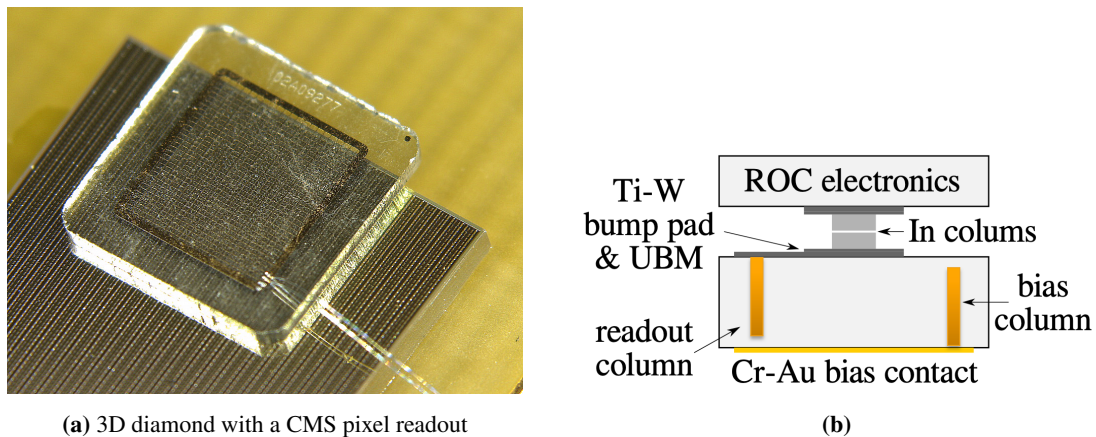


Figure 3: A photograph (left) and a cross section schematic (right) of a 3D pixel detector bump bonded to a pixel readout chip.

After assembly, the detectors were tested in several beam tests at three different test facilities. At the test facility of the Paul Scherrer Institute (PSI) the devices were tested with 260 MeV positive pions, at CERN the beam consisted of 120 GeV hadrons, at DESY a beam of 4 GeV electrons was utilized. In all the tests the detector under test (DUT) was placed inside a beam telescope that was used for reconstruction of the particle tracks and prediction of the position of their hits on the DUT. Also, in all the tests the bias applied to the bias columns was always negative and the readout columns were connected to the AC ground through the front-end electronics.

3. Results

The plots of the average pulse height in this section are normalized to value at the 95% quantile, in order to ease the comparison of the patterns in the plots.

The average pulse height versus the predicted hit position plots (Figure 4) show a noticeable difference between the detectors with $50\ \mu\text{m}\times 50\ \mu\text{m}$ (Fig. 4a) and $100\ \mu\text{m}\times 150\ \mu\text{m}$ (Fig. 4b) cells. The average pulse height of the detector with $50\ \mu\text{m}\times 50\ \mu\text{m}$ ganged cells shows the pattern typical for polycrystalline diamond detectors. The spatial variations in the pulse height are due to the variations in the collected charge of different grains. However, in the detector with the $100\ \mu\text{m}\times 150\ \mu\text{m}$ cells, where each cell is read out by an individual pixel, the pattern follows the pixel structure. In several places the 3D electrodes are missing. Most of those places are located at the periphery of the 3D region. In those areas the signals do not pass the threshold and the hits are not registered. Thus, one observes blanks (lack of hits) in these locations. The blank rectangle in the center of the plot in Figure 4b is due to a faulty pixel in the reference plane of the telescope, which prevented the reconstruction of tracks at this location. For the further analysis, only the hits in the fiducial regions (indicated by the red rectangles on the plots) were chosen in order to avoid the problem areas at the periphery.

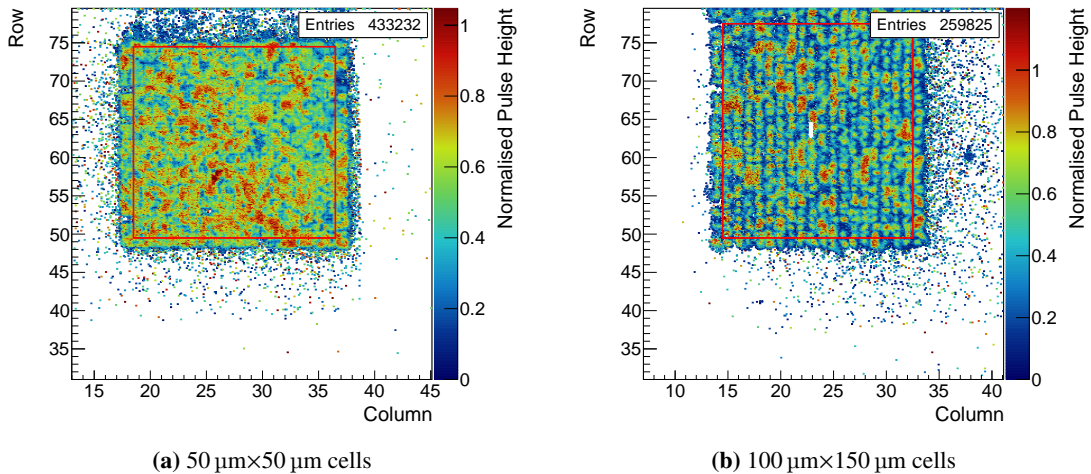


Figure 4: Average pulse height versus the predicted hit position for detectors with $50\ \mu\text{m}\times 50\ \mu\text{m}$ cells at $-55\ \text{V}$ bias (left) and $100\ \mu\text{m}\times 150\ \mu\text{m}$ cells at $-50\ \text{V}$ bias (right). The red square outlines the fiducial area.

The maps of the cluster size versus the predicted hit position within a pixel (Figure 5) show larger cluster size at the edges and at the corners of the pixel. This pattern is expected, due to the charge sharing between the pixels. The reason for larger cluster size between the rows than between the columns of the device with $50\ \mu\text{m}\times 50\ \mu\text{m}$ cells is not understood but is suspected to be due to a specific tuning of the readout chip.

The efficiency maps versus the predicted hit position for the detector with $50\ \mu\text{m}\times 50\ \mu\text{m}$ cells (Figure 6a) displays mostly uniform efficiency with a slightly lower efficiency around the bias columns (indicated by the black dots), especially around the bias columns on the horizontal periphery of the pixel. The lower efficiency at the periphery is likely due to the charge sharing between the pixels. The induced charge is split between the two pixels, thus each pixel has only a

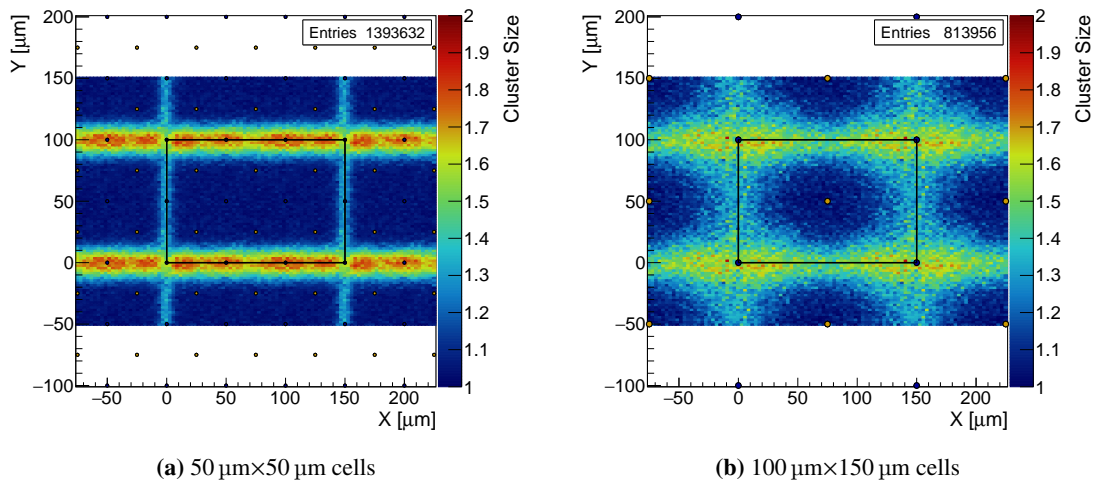


Figure 5: Cluster size versus predicted hit position within a pixel for detectors with $50\ \mu\text{m}\times 50\ \mu\text{m}$ cells at $-55\ \text{V}$ bias (left) and $100\ \mu\text{m}\times 150\ \mu\text{m}$ cells at $-50\ \text{V}$ (right). The locations of bias electrodes are indicated by black dots and the locations of the readout cells are indicated by yellow dots.

fraction of the charge while still needing to pass the threshold in each pixel in order to be detected. The lower efficiency around the bias electrodes that are not on the periphery is not yet understood.

The efficiency map for the detector with $100\ \mu\text{m}\times 150\ \mu\text{m}$ cells displays highly non-uniform efficiency. The lower efficiency along the vertical edges of the cells can be partially explained by the charge sharing between the pixel and partially by the longer drift distance, due to the larger cell size, and therefore a higher trapping probability of the carriers.

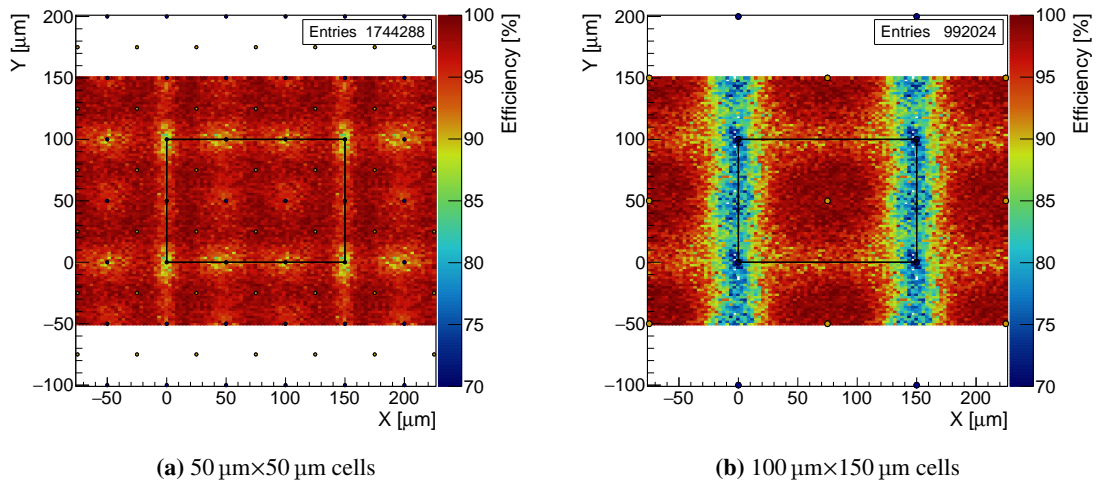


Figure 6: Efficiency versus predicted hit position within a pixel. The detector with $50\ \mu\text{m}\times 50\ \mu\text{m}$ cells is biased at $-55\ \text{V}$ (left) and the detector with $100\ \mu\text{m}\times 150\ \mu\text{m}$ cells is biased at $-50\ \text{V}$ (right). The locations of bias electrodes are indicated by black dots and the locations of the readout cells are indicated by yellow dots.

The plots of the average pulse height versus the predicted hit position within the pixel (Figure 7) manifest patterns very similar to the efficiency maps. The pulse height is higher in the areas with higher efficiency and lower in the areas with lower efficiency. The difference is observed only next

to the bias electrodes along the horizontal edge of the pixel for the detector with $50\ \mu\text{m}\times 50\ \mu\text{m}$ cells (Figure 7a). It can be explained by the prevalence of the two pixel clusters there (Figure 5a) that artificially raises the pulse height by requiring the signal in both pixels to cross the threshold, raising the lower tail of the pulse height distribution. The average pulse height pattern manifested by the detector with $100\ \mu\text{m}\times 150\ \mu\text{m}$ cells (Figure 7b) shows an even stronger effect than in the efficiency plot of the distance to the readout electrode on the induced signal.

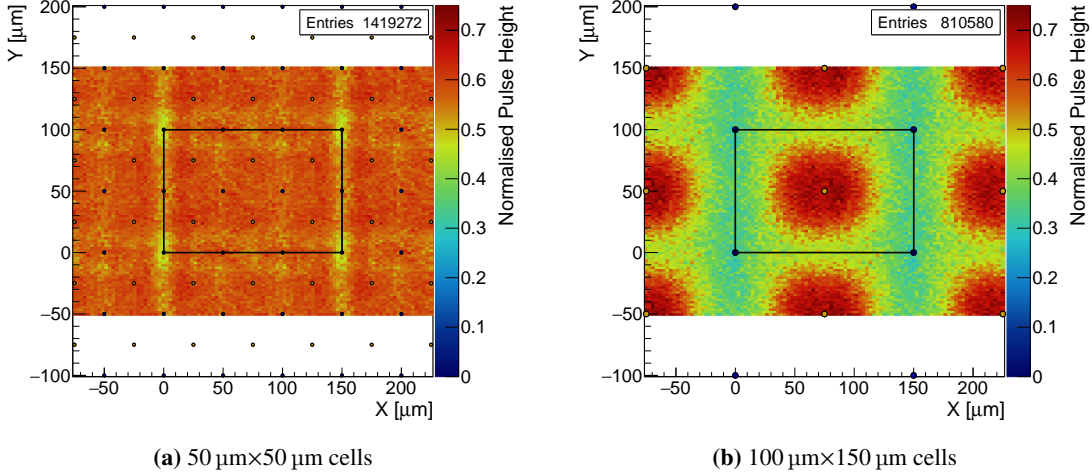


Figure 7: Average pulse height versus predicted hit position within a pixel for detectors with $50\ \mu\text{m}\times 50\ \mu\text{m}$ cells at $-55\ \text{V}$ bias (left) and $100\ \mu\text{m}\times 150\ \mu\text{m}$ cells at $-50\ \text{V}$ (right). The locations of bias electrodes are indicated by black dots and the location of the readout cells are indicated by yellow dots.

The efficiency of the detectors within the fiducial region was also studied with respect to the bias voltage (Figure 8a). Unlike in the tests that resulted in the plots shown above, the threshold for this study was set to a value of ~ 2000 electrons. As expected, the efficiency of the detector with the smaller ($50\ \mu\text{m}\times 50\ \mu\text{m}$) cells reaches saturation at a much lower bias than the efficiency of the detector with larger ($100\ \mu\text{m}\times 150\ \mu\text{m}$) cells. The maximum efficiency reached by the detector with the $50\ \mu\text{m}\times 50\ \mu\text{m}$ cells was 99.2% at $-50\ \text{V}$.

The pulse height distribution of the 3D diamond detector with $50\ \mu\text{m}\times 50\ \mu\text{m}$ cells at $-55\ \text{V}$ bias (see Figure 8b) poses overall characteristics of a Landau distribution, however, it is slightly broader and has larger tail on the lower side. The comparison with the pulse height distribution of $285\ \mu\text{m}$ thick silicon pixel detector biased at $-150\ \text{V}$, which was tested in parallel with the 3D diamond detector, allows for a rough calibration of the pulse height scale. By applying this calibration we estimate that $>70\%$ of the induced charge was collected by the 3D diamond detector.

4. Conclusions

The research performed by the RD42 collaboration further advances the understanding of the diamond detector and helps to advance their usage in high energy physics experiments. The highlights of this research were presented. It was shown that the pulse height of the irradiated pCVD diamonds does not depend on the particle flux within the range from $3\ \text{kHz cm}^{-2}$ to $20\ \text{MHz cm}^{-2}$ up to the fluence of $2 \cdot 10^{15}\ \text{n cm}^{-2}$. The 3D electrodes in a $500\ \mu\text{m}$ thick pCVD diamond were

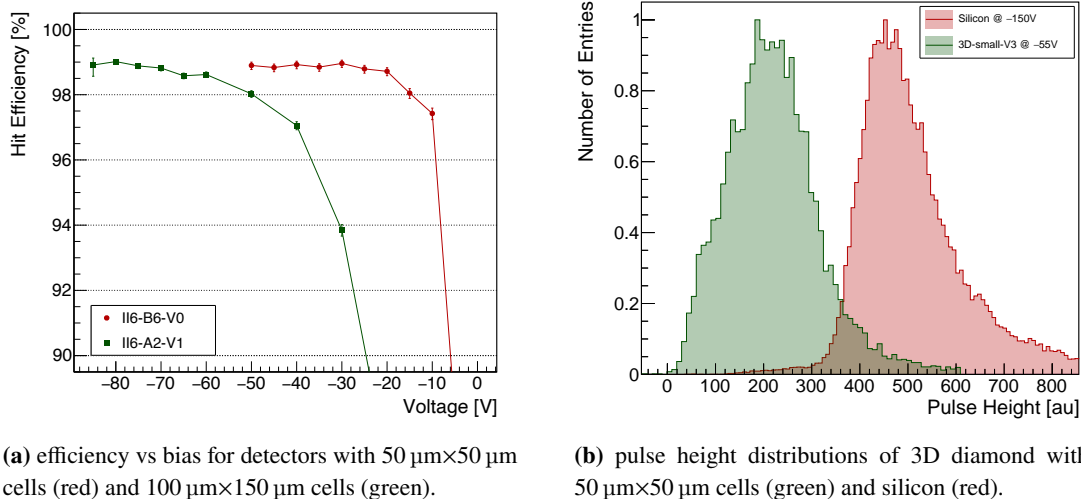


Figure 8: The comparison of efficiencies versus bias of two 3D diamond detectors, and pulse height distributions of the 3D diamond detector with $50\ \mu\text{m}\times 50\ \mu\text{m}$ cells and a $285\ \mu\text{m}$ thick silicon detector.

produced with the help of a femtosecond laser with efficiency of 99.7% and a diameter of $2.6\ \mu\text{m}$. The beam test performed on the 3D detectors indicated that $100\ \mu\text{m}\times 150\ \mu\text{m}$ 3D cells are too large to efficiently collect the charge. In comparison, the smaller $50\ \mu\text{m}\times 50\ \mu\text{m}$ 3D cells demonstrated more uniform efficiency and pulse height. A further reduction of the cell size to $25\ \mu\text{m}\times 25\ \mu\text{m}$ will likely result in even higher charge collection efficiency and in addition will likely provide a better radiation tolerance. The electrode diameter of $2.6\ \mu\text{m}$ is small enough for the cell of that size and will not reduce the efficiency by introducing the inactive material. The RD42 collaboration plans to produce and test the performance of such 3D detectors up to fluences of $2 \cdot 10^{16}\ \text{n cm}^{-2}$.

Acknowledgments

The RD42 Collaboration gratefully acknowledges the staff at CERN for test beam time and their help in setting up beam conditions. We would especially like to thank Barbara Holzer, the CERN test beam coordinator, and André Rummler for their assistance in making our tests a success in H6a. The authors would also like to thank the πM1 beam line staff at the PSI High Intensity Proton Accelerator. The measurements leading to these results have been performed at the Test Beam Facility at DESY Hamburg (Germany), a member of the Helmholtz Association (HGF). The authors would like to acknowledge the Princeton University Materials Institute (PMI), Micro Fabrication laboratory (MNFC) and Bert Harrop for the efforts in metallization and bump-bonding. The research leading to these results received funding from the European Union's Horizon 2020 research and innovation program under grant agreement No. 654168. This work was also partially supported by Swiss National Science Foundation Grant #20FL20_154216, ETH Grant 51 15-1, Swiss Government Excellence Scholarship ESKAS No. 2015.0808, UK Science and Technology Facilities Council Grant ST/M003965/1, Slovenian Research Agency (grant No. J1-3032 and P1-0135) and U.S. Department of Energy Grant DE-SC0011726.

References

- [1] A.J. Edwards and et al. [BABAR Collaboration], *Radiation monitoring with diamond sensors in BABAR*, *IEEE Transactions on Nuclear Science* **51** (2004) 1808.
- [2] R. Eusebi and et al. [CDF BCM Collaboration], *A diamond-based beam condition monitor for the CDF experiment*, *2006 IEEE Nuclear Science Symposium Conference Record 2* (2006) 709.
- [3] A. Gorišek and et al. [ATLAS BCM Collaboration], *ATLAS diamond beam condition monitor*, *Nuclear Instruments and Methods in Physics Research Section A: Accelerators, Spectrometers, Detectors and Associated Equipment* **572** (2007) 67 .
- [4] A.J. Bell and et al. [CMS Collaboration], *Beam and radiation monitoring for CMS*, in *2008 IEEE Nuclear Science Symposium Conference Record*, pp. 2322–2325, 2008, DOI.
- [5] M. Domke and et al. [LHCb BCM Collaboration], *Commissioning of the beam conditions monitor of the LHCb experiment at CERN*, in *2008 IEEE Nuclear Science Symposium Conference Record*, pp. 3306–3307, Oct, 2008, DOI.
- [6] L. Bäni and et al. [RD42 Collaboration], *A study of the radiation tolerance of poly-crystalline and single-crystalline CVD diamond to 800 MeV and 24 GeV protons*, *Journal of Physics D: Applied Physics* **52** (2019) 465103.
- [7] L. Bäni and et al. [RD42 Collaboration], *A study of the radiation tolerance of CVD diamond to 70 MeV protons, fast neutrons and 200 MeV pions*, *Sensors* **20** (2020) 6648.
- [8] M. Reichmann, *A Particle Tracker for an Extreme Radiation Environment with Strongly Changing Fluxes*, Ph.D. thesis, ETH-28688, 2022.
- [9] S. Parker, C. Kenney and J. Segal, *3D - A proposed new architecture for solid-state radiation detectors*, *Nuclear Instruments and Methods in Physics Research Section A: Accelerators, Spectrometers, Detectors and Associated Equipment* **395** (1997) 328 .
- [10] F. Bachmair and et al. [RD42 Collaboration], *A 3D diamond detector for particle tracking*, *Nuclear Instruments and Methods in Physics Research Section A: Accelerators, Spectrometers, Detectors and Associated Equipment* **786** (2015) 97 .
- [11] B. Sun, P.S. Salter and M.J. Booth, *High conductivity micro-wires in diamond following arbitrary paths*, *Applied Physics Letters* **105** (2014) 231105
[<https://doi.org/10.1063/1.4902998>].
- [12] B. Harrop, *Princeton bump bonding*, 2021.
- [13] *psi46dig pixel chip external specification manual*, 2021.